Chinese Journal of Aeronautics, (2016), 29(4): 893–913

Chinese Society of Aeronautics and Astronautics
& Beihang University

Chinese Journal of Aeronautics

cja@buaa.edu.cn
www.sciencedirect.com

Characterization of component interactions in two-stage axial turbine

Adel Ghenaiet [a,*], **Kaddour Touil** [b]

[a] *Laboratory of Energetics and Conversion Systems, Faculty of Mechanical Engineering, University of Sciences and Technology Houari Boumediene, BP32 El-Alia Bab-Ezzouar, 16111 Algiers, Algeria*
[b] *Laboratory of Thermal Power Systems, Applied Mechanics, EMP BP17 Bordj-el-Bahri, 16046 Algiers, Algeria*

Received 26 February 2015; revised 25 January 2016; accepted 11 April 2016
Available online 22 June 2016

KEYWORDS

CFD;
FFT analysis;
Pressure fluctuations;
Two-stage axial turbine;
Unsteady flows;
Vane/blade interactions

Abstract This study concerns the characterization of both the steady and unsteady flows and the analysis of stator/rotor interactions of a two-stage axial turbine. The predicted aerodynamic performances show noticeable differences when simulating the turbine stages simultaneously or separately. By considering the multi-blade per row and the scaling technique, the Computational fluid dynamics (CFD) produced better results concerning the effect of pitchwise positions between vanes and blades. The recorded pressure fluctuations exhibit a high unsteadiness characterized by a space–time periodicity described by a double Fourier decomposition. The Fast Fourier Transform FFT analysis of the static pressure fluctuations recorded at different interfaces reveals the existence of principal harmonics and their multiples, and each lobed structure of pressure wave corresponds to the number of vane/blade count. The potential effect is seen to propagate both upstream and downstream of each blade row and becomes accentuated at low mass flow rates. Between vanes and blades, the potential effect is seen to dominate the quasi totality of blade span, while downstream the blades this effect seems to dominate from hub to mid span. Near the shroud the prevailing effect is rather linked to the blade tip flow structure.
© 2016 Chinese Society of Aeronautics and Astronautics. Production and hosting by Elsevier Ltd. This is an open access article under the CC BY-NC-ND license (http://creativecommons.org/licenses/by-nc-nd/4.0/).

1. Introduction

Axial turbines of modern aero-engines are designed at high loading factors, hence leading to inherently complex flows which are in essence unsteady owing to the relative motion between nozzle guide vanes (NGV) and rotor blades. Each row generates non-uniformities in the downstream flow field due to potential and viscous effects which are ingested by the following vanes/blades' rows. Among the most important non-uniformities in the case of hp turbines are wakes, secondary flows, shocks and hot-streaks. Early flow models used

* Corresponding author.
E-mail address: ag1964@yahoo.com (A. Ghenaiet).
Peer review under responsibility of Editorial Committee of CJA.

http://dx.doi.org/10.1016/j.cja.2016.06.007
1000-9361 © 2016 Chinese Society of Aeronautics and Astronautics. Production and hosting by Elsevier Ltd.
This is an open access article under the CC BY-NC-ND license (http://creativecommons.org/licenses/by-nc-nd/4.0/).

simplifying assumptions such as the through-flow[1] methods neglecting the circumferential variations and unsteadiness related to the relative motion between rotating and stationary parts. After advents of CFD tools, and since experiments are cumbersome and in many cases impossible, it has become presumably possible to predict the details of flow structures and direct investigations towards the most challenging unsteady phenomena, especially the stator/rotor interactions.

The flow computations based on one blade per row is still used when predicting the turbomachinery performance. However, Dieter and Jing[2] have concluded that with a computational domain restricted to one blade, there is a variation in the turbine stage efficiency about 0.52% among different clocking positions. Therefore, there is still a need for reducing the computational domain in multi-component machinery without affecting too much the flow physics. In this issue many workers accounted for the non-integral blade counts, such as Erdos et al.[3] who first developed the "phase lagged method" to compensate for the non-integral blade counts without modeling the entire blades rows. Adamczyk[4] after introducing the mixing-plane method[5] proposed the average-passage method in which the rotor domain is expanded upstream and downstream. Giles[6] modified the "phase lagged method" and eliminated the assumption of temporal periodicity by using the time inclined computational plane. A way of calculating rotor-wake interaction is to use ordinary unsteady CFD with the time lagged periodic boundary condition, i.e., the chorochronic periodicity[7,8] and the Fourier representation near periodic boundaries. Gerolymos et al.[8] gave a detailed analysis of the chorochronic periodicity and proposed a new methodology for predicting the unsteady aerodynamics of the interactions between two blade rows based on Fourier series both in time and circumferential direction. By comparing with the measurements made for a 1.5 stage turbine, the ability of this technique in studying stator/rotor interactions was clearly shown. Miller et al.[9] studied the interaction of an hp transonic turbine stage followed by an intermediate vane, focusing on the upstream potential effects of the vanes on the rotor blades, which seemed to be only affected downstream the throat. Later, Miller et al.[10] described accurately the flow structure of vane and the shock/wake interaction and migration of flow across the rotor and the interference of both rotor and second vane potential fields on the coming flow.

Rai and Madavan[11] concentrated their study on the scaling technique to overcome the problem of non-integral blade counts by scaling the blade pitch while maintaining a constant solidity ratio. Arnone and Pacciani[12] carried out the domain scaling technique for a two-stage transonic turbine having 22 vanes and 38 blades. The scaled configurations were successively: 1/2 (scaling ratio 0.87), 3/5 (scaling ratio 1.036), 4/7 (scaling ratio 0.987) and 7/12 (scaling ratio 1.0076). Their conclusion is that the 1/2 configuration led to a premature choking in the rotor passages and the pressure distributions were significantly affected, but these effects were largely reduced in the 3/5 configuration and even nonexistent in the 4/7 configuration. Clark et al.[13] and Yao et al.[14] have shown the importance of modeling the actual blade counts in multi-stage simulations for accurate predictions of the entropy migration and the frequency spectrum resulting from stator/rotor interactions. Clark et al.[13] investigated the effect of blade count and scaling on the unsteady pressure field for a configuration of an axial turbine representative of a modern design, consisting of 36 vanes and 56 blades of the hp stage and 36 vanes of the lp stage. They showed that as the scaling was used (holding the mid-span axial gap) to reduce the computational domain to only 2 vanes and 3 blades for the first stage and 2 vanes for the second stage (1/18th of wheel), errors in the unsteady pressure amplitudes could arise. Also Yao et al.[14], based on simulations for a 1.5 stage axial turbine of vane/blade counts 36, 41 and 36, showed that for the configurations 6/7/6 (scaling ratio 0.9762) and 1/1/1 (scaling ratio 1.14), the time-averaged pressure distributions over the vanes and blades were not significantly affected, and concluded that the scaling ratio should be kept close to unity. He and Chen[15] applied the unsteady Navier–Stokes equations to analyze the stator/rotor interactions in an axial turbine with 32 vanes and 48 blades, and concluded that the computational domain consisting of 2 vanes and 3 blades produced unsteady pressures that were compared well with the experimental data. The aforementioned studies showed a veritable challenge for the CFD codes in providing acceptable details of the main flow features, especially the stator/rotor interactions which involves the potential interaction propagating both upstream and downstream. The magnitude of this effect depends on the Mach number and the axial inter-distance. Unlike the potential influence, the blade wake is only convected downstream and the static pressure does not vary significantly. In the transonic regime, shock structure provokes intense unsteady effects. The most significant contribution to unsteadiness is the periodic chopping of wakes[16] and secondary flow vortices from the upstream blade row by the downstream blade row.[17,18] Also the interactions of convected secondary flow vortex/tip leakage vortex with the periodic wake or potential field should be considered. According to the literature there are few published works on the unsteady interactions between leakage flows and adjacent vane/blade rows in axial turbines. Behr et al.[19] have indicated that the pressure field of the second vane has an influence on the development of tip leakage vortex of the rotor. Qi and Zhou [20] performed an experimental and a numerical investigation in the blade tip region and concluded that the upstream wakes are shown to reduce the strength of the tip leakage vortex, and owing to the unsteady effects of wakes there is appearance of counter-rotating vortex pairs within the tip leakage vortices which cause a significant pressure fluctuation.

This study concerns the determination of aerodynamic performance of an hp two-stage axial turbine and the analysis of stator/rotor interactions by means of the code Ansys-CFX. Because the computing power was very limited, the technique of domain scaling was applied to reduce the computational domain and grid size. This latter required a careful treatment for the blade profiles and aspect ratio while adopting a scaling ratio close to unity in order to conserve the physical periodicity and not altering too much the aerodynamic performance. The fluctuations of static pressure were recorded at different points and lines and the FFT was used to analyze the flow unsteadiness characterized by a space–time periodicity, leading to the determination of different frequencies and spatial modes characterizing these interactions.

2. Geometry and computation grids

This two-stage hp axial turbine (Fig. 1) drives an hp compressor of an old turbofan engine. The determination of the

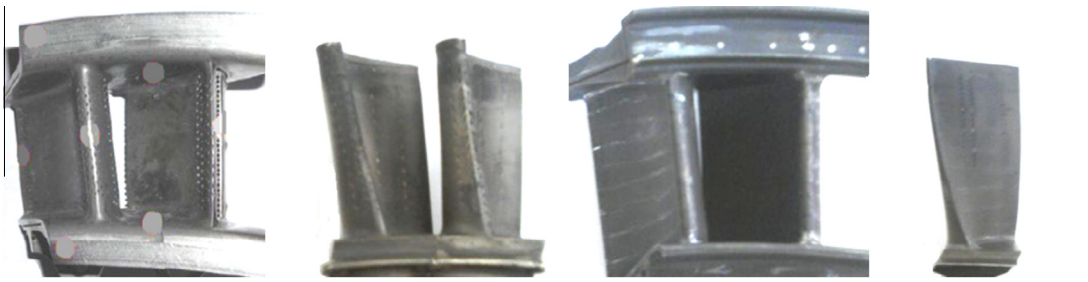

(a) 1st stage NGV (b) 1st stage blade (c) 2nd stage NGV (d) 2nd stage blade

Fig. 1 The two-stage hp axial turbine components.

geometry of the two stages vanes and blades required utilizing an optical measuring machine equipped with a contact-less optical feeler and a three-jaw chuck to rotate and sweep the totality of measured surfaces. The main data are given in Table 1 and the CAD models are shown by Fig. 2.

The grids of the vanes and rotor blades required the topology of different blocks to be arranged in regular (structured) and irregular (unstructured) patches meshed by hexahedral elements with an H-grid type at leading edge and J-grid at trailing edge. An O-grid guaranteed near-orthogonal elements and a better resolution of boundary layers around vanes and blades and a clustering near the hub and blade tip allowing a good resolution of the flow gradients and the vortical structures. Local refinements to boundary layers required values of y^+ compatible with the turbulence model k–ω SST which has been validated in various turbomachinery applications and produced excellent results, particularly with regard to flow separations. The near wall distance was estimated based on the first node distance[21] $y_p = 357.77\ \bar{c}Re_c^{-0.92}$, and to cover regions of high Reynolds number, the maximum of flow velocity was used. After a preliminary assessment of grid refinements under the nominal operating conditions, corrections for the near wall distances were made and the steady simulations were repeated to assess the final quality of the grids. To study the dependency of flow solution on the mesh sizes, the total-to-total isentropic efficiency η_{ttis} is plotted (Fig. 3) against six grid sizes, showing a stability of solution above a grid size of 653,344 nodes which was considered for the next computations. The different grids are presented in Fig. 4 and the meridional view is shown by Fig. 5.

Table 1 Main characteristics of hp two-stage axial turbine.

Characteristics	Dimension (mm)			
	1st NGV	1st rotor	2nd NGV	2nd rotor
Blade count	46	80	56	74
Inlet hub diameter	737	727	720	686
Inlet shroud diameter	836	836	836	864
Outlet hub diameter	727	720	686	682
Outlet shroud diameter	836	836	864	864
Average blade height	52	56.25	73.5	90
Tip clearance		2.146		2.146

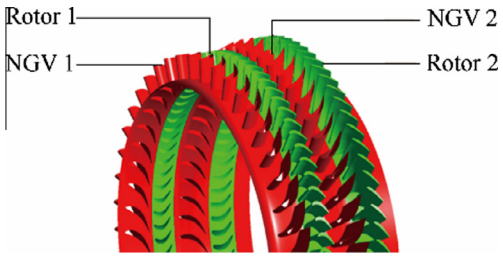

Fig. 2 CAD of the two-stage axial turbine.

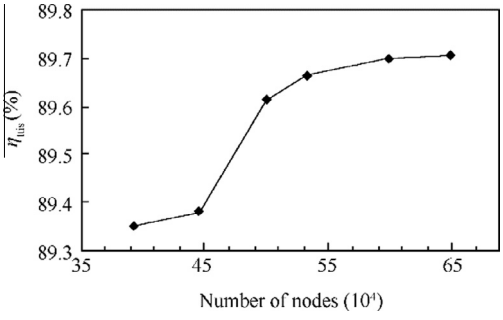

Fig. 3 Grid size dependency.

3. Steady flow simulations

The steady flow simulations were carried out by means of the code Ansys-CFX, under the operating conditions corresponding to averaged inlet total pressure P_{t0} = 2,841,460 Pa and temperature T_{t0} = 1510 K, while the rotational speed was varied around the nominal value of 9823 rpm.[22] The frozen rotor interface is useful when the circumferential variations of flow properties are large. In such an interface, the stationary and rotating frames are connected so that each sliding interface has a fixed relative position for producing the steady solution to the multiple frames and accounting for interactions between them. The stage interface appropriately used in predicting the aerodynamic performance does not require the interfaces to be identical on both sides, and the averaging incurs a one-time mixing loss equivalent to assuming that the physical mixing supplied by the relative motion between the components is sufficiently large to cause any upstream velocity profile to mix out prior entering the downstream component.

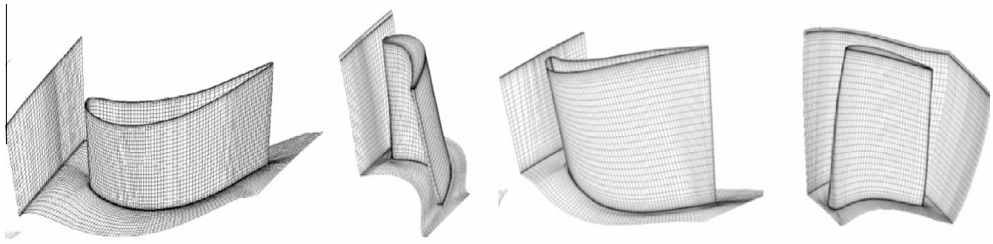

Fig. 4 The components grids.

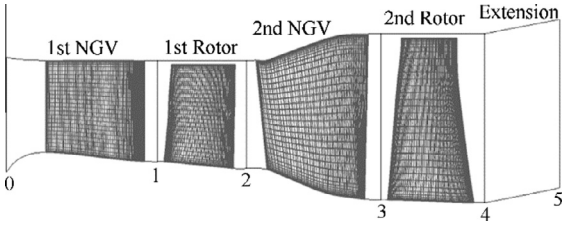

Fig. 5 Meridional view of the different grids.

3.1. One-blade per passage simulations

Here, the averaged inlet total pressure and temperature were imposed at inlet of first NGV and a static pressure was specified at exit of second rotor, while the periodic boundary condition applied at one pitch away of each component. The high resolution advection scheme with a local time scale factor of 10 was used for the flow simulations. The predicted aerodynamic performance maps based on the stage interface are given in terms of total-to-total isentropic efficiency η_{ttis} and total-to-total expansion ratio π_{tt} as function of reduced mass flow parameter $\dot{m}\sqrt{T_{t0}}/P_{t0}$, for different rotational speeds of $N = 30$–107.4% of the nominal speed N_n.

First, the aerothermodynamic performance of the two-stage axial turbine (Fig. 6(a)) depicts a limited operating range at the highest speed of; rotation. The peak of total-to-total isentropic efficiency η_{ttis} increases slightly for each rotational speed, and the maximum efficiency reaches a value of 88.43% for a reduced mass flow parameter of 1.552×10^{-3} (mass flow rate of 113.5 kg/s) at a rotational speed of 107.4%. The predicted expansion ratio with rotational speed depicts curves practically superimposed and become steep at high mass flow rates to reach the choking limit having a critical value that varies with the speed of rotation. The performance maps of the first stage (Fig. 8(b)) depict a slight increase in the peak of efficiency with rotational speed, and the curves of expansion ratio are distinguishable at low mass flow rates. The design point seen at a peaked efficiency of 92.06% corresponds to a reduced mass flow parameter of 1.42×10^{-3} (mass flow of 104 kg/s) and a rotational speed of 107.4% nominal speed. According to the curves of efficiency, the operating range of the first stage is wider compared to the two-stage hp turbine. On the other hand, the performance maps of the second stage (Fig. 8(c)) are strongly influenced by flow non-uniformities imposed by the first stage that caused an increase in entropy convected through the next components. At low mass flow rate the difference in the curves of expansion ratio is more noticeable. The peak of efficiency reaches a value of 91.42% for a reduced mass flow parameter of 3.1×10^{-3} (mass flow of 112.89 kg/s) at a rotational speed of 100% nominal speed.

For the nominal operating point ($N = 10{,}550$ rpm and $m = 113.5$ kg/s), the evolutions of average expansion properties based on mass averaging exhibit a large drop in total pressure through the first rotor which is more loaded than the second one. Fig. 7(a) depicts the streamwise variation of average static pressure through this reaction turbine which has an estimated reaction rate equal to 26.5% for the first stage and 69.5% for the second stage. The average Mach number (Fig. 7(b)) shows flow acceleration through first NGV reaching a supersonic velocity beyond the throat. With respect to rotating blades, the flow is more accelerated through the second rotor of a higher rate of reaction.

The spanwise distributions of static pressure as plotted (Fig. 8a) over the meridional planes of vanes and blades depict a clear drop in static pressure through the components, especially the first NGV. The flow velocity is seen to decrease from hub to shroud of first NGV, but on the contrary, in the second one it increases upward followed by an abrupt drop near the shroud. High pressure loading is seen over the blades and the flow is accelerated to reach a sonic speed at throat, even higher towards the tip due to circumferential speed. The flow behavior in the second rotor is largely affected by the flow structures of the upstream components.

The flow streamlines colored by the relative flow velocity and plotted on blade-to-blade planes (Fig. 9) show that the flow is well guided except towards the tip where the leakage flow and local vortices deflect the flow from pressure side to suction side of blade. The tip leakage flow occurs as a result of pressure difference forcing the main flow to generate the tip leakage vortex and horseshoe vortex emanating from the leading edge and extending farther to interact with the downstream vane and initiate hot spots in its tip region. The flow across the first vane is well guided except near the hub (Fig. 10(a)) where a bubble is formed added to secondary flows from the suction side. A part of the vane's wake is ingested to cause a flow deviation at the blade leading edge of blade, thereby inducing a large disturbance to the flow incidence. In the first rotor blade, the streamlines (Fig. 10(b)) are seen to deviate in the spanwise direction, leading to the formation of hub passage vortex. The wake induced by first rotor blade as well as the tip leakage flow and the vortices impose a negative flow incidence towards the second vane, resulting in the formation of a large vortex which disturbs the flow towards the second rotor blade. Moreover, the secondary flows (Fig. 10(c)) deflect streamlines towards the hub and shroud over the pres-

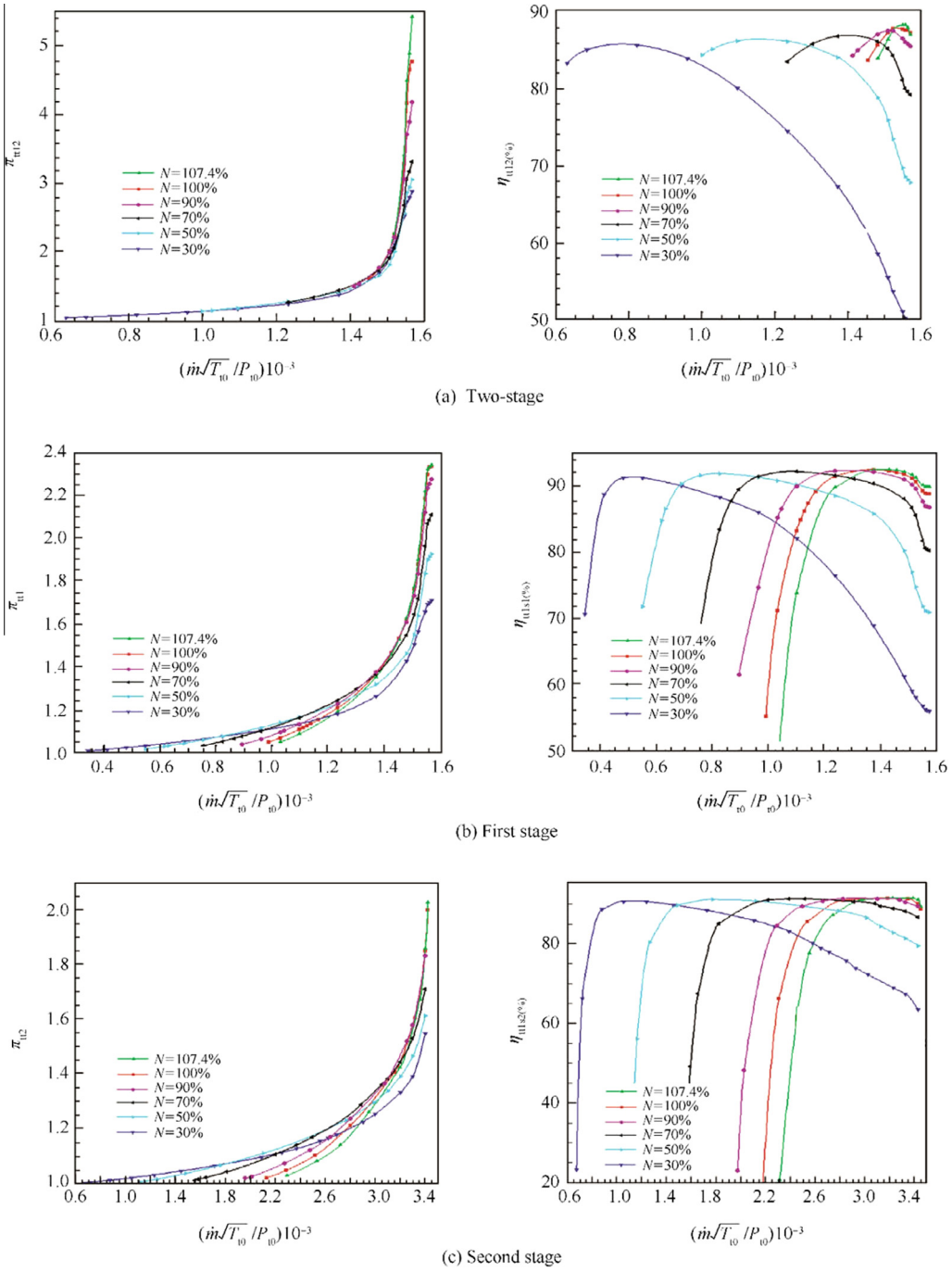

Fig. 6 Performance maps (total-to-total expansion ratio and total-to-total isentropic efficiency).

sure side and towards the mid-span of suction side. In the second rotor blade (Fig. 10(d)) the flow structure, largely affected by the previous components, is characterized by the leakage flow and the horseshoe vortex enveloped by the leakage vortex which mixes out with the annulus wall boundary layer.

The meridional distribution of entropy (Fig. 11(a)) reveals an increase in losses at the throat of first vane. The wake and the vortex shedding over blade tip and the boundary layers at endwalls of first rotor blade (Fig. 11(b)) appear clearly as sources of entropy generation. The maximum of entropy is seen near the casing as a result of strong tip leakage vortex created by the first and second rotor blades. The effect of tip leakage vortex from first rotor blade is felt in the second NGV causing a high flow incidence and participating in generating a vortex flow at the shroud corner. In the second rotor the effect of tip leakage vortex is more intense compared to the first rotor.

3.2. Multi-blade passage simulations

The scaling technique is based on the principle of modifying for each row the blade count and the chord and thickness of blade while conserving the solidity and the circumferential periodicity. For not affecting too much the flow structures

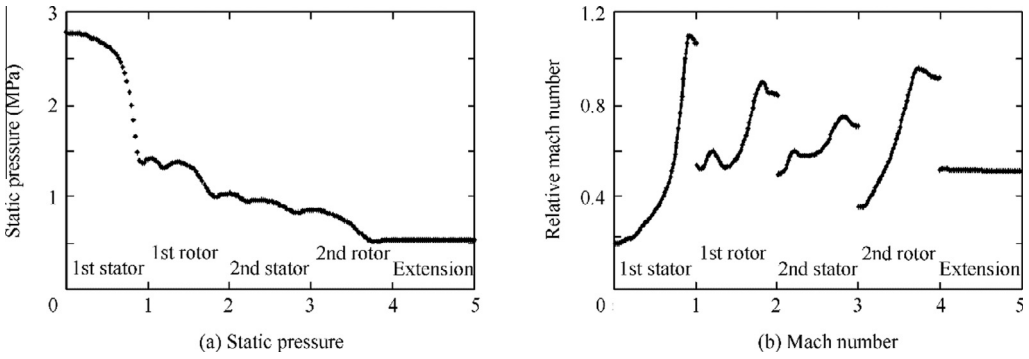

Fig. 7 Evolutions of expansion properties.

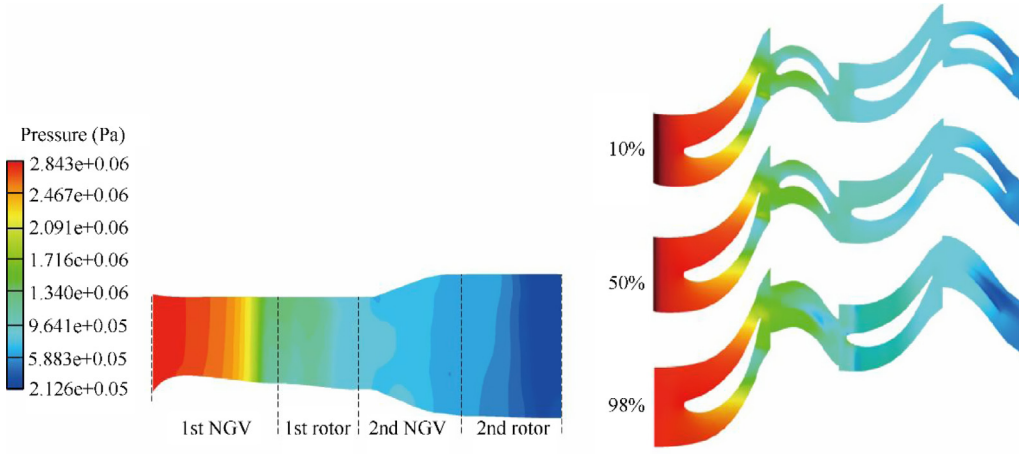

(a) Meridional plane **(b)** Different spans

Fig. 8 Static pressure distribution.

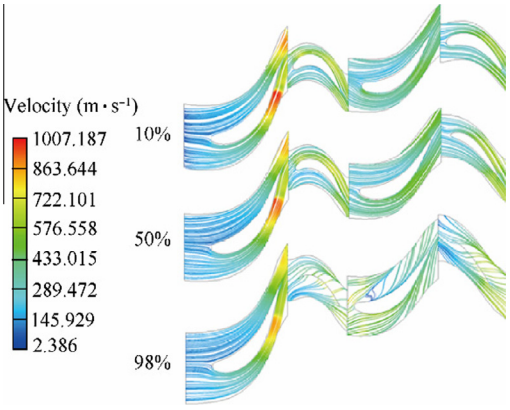

Fig. 9 Streamlines colored by the relative flow velocity at different spans.

and the unsteady behavior by changing the frequencies of interactions, it is necessary to make these modifications as weak as possible and use low values of the scaling factors. To satisfy these considerations, the computational domain was modified to the new configuration of 4/7/5/7 passages; that means 4 vanes and 7 blades for the first stage and 5 vanes and 7 blades for the second stage. In order to keep the true periodicity at the angle of 31.5°, the scaling ratios used for the vane and blade of the first stage are both equal to 1, whereas for the second vane and blade the scaling ratios are equal to 1.018 and 1.081, respectively. The new computational domain is generated under CFX-Pre using the transform mesh option to create the multiple vanes and blades passages, hence resulting in a total grid size of 3,834,245 nodes which suited our computing resources.

The plot of static pressure at different blade-to-blade planes (Fig. 12) show that the leading edges of blades are not loaded the same, especially the first rotor. Also, the distributions of relative Mach number (Fig. 13) exhibit supersonic regions downstream of first NGV which are not periodic. In first rotor, the regions of accelerated flow are not repeating and the wakes originated from vanes do not overlap all the rotor blades. The circumferential variations are more illustrated in the second rotor due to the convected wakes from upstream components and the vortex structure near the second NGV casing.

As seen from Fig. 14, the wakes convected downstream of vanes and blades are the major sources of entropy creation. The wakes are chopped into segments by the downstream blade row and are not periodically enveloping the rotor blades, and behave as a negative jet impinging on the blades which affects the aerodynamic blade loading. Indeed, because of velocity deficit in wakes, the inlet flow angles to the next row are changed. Interactions with the second NGV lead to cir-

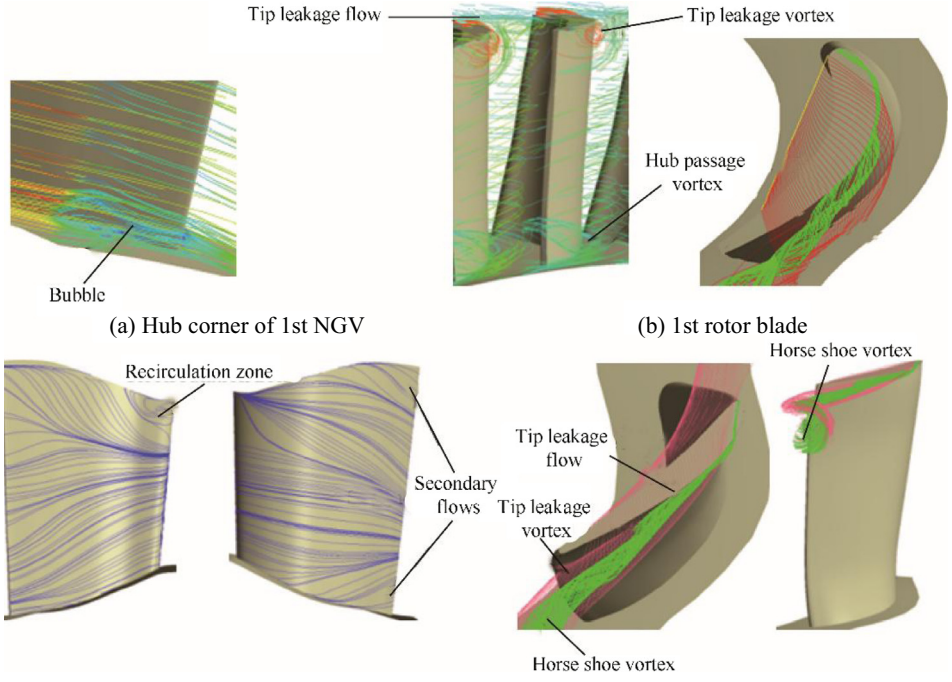

Fig. 10 Details of flow structure.

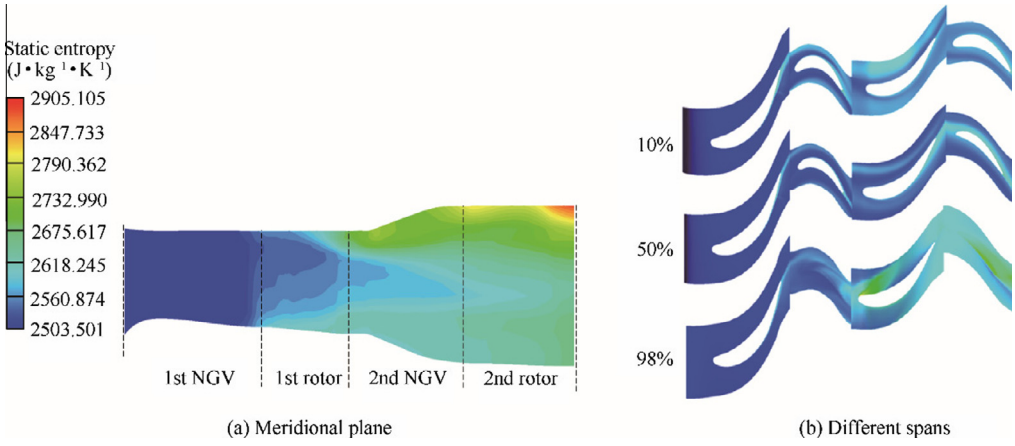

Fig. 11 Static entropy distribution.

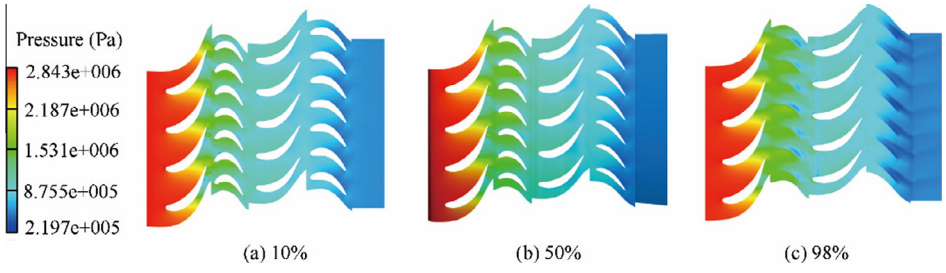

Fig. 12 Static pressure at different spans.

cumferential flow distortions which are more accentuated in the second rotor. As seen from Fig. 15(a), the distribution of static entropy at exit of first NGV exhibits a circumferential distortion reaching its maximum at hub corner where secondary flows develop. The distribution of static entropy at exit of first rotor (Fig. 15(b)) depicts the formation of wakes and

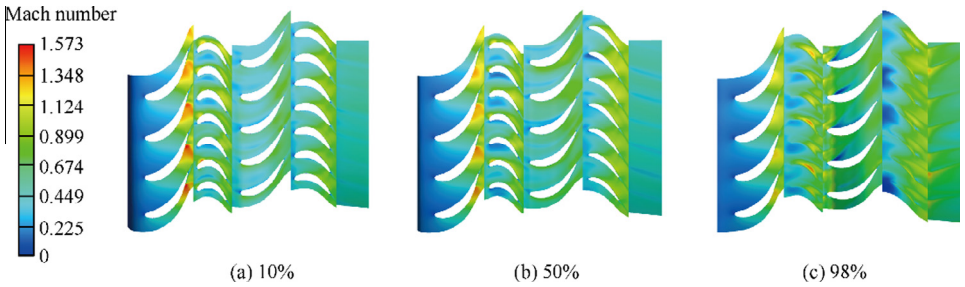

Fig. 13 Relative Mach number at different spans.

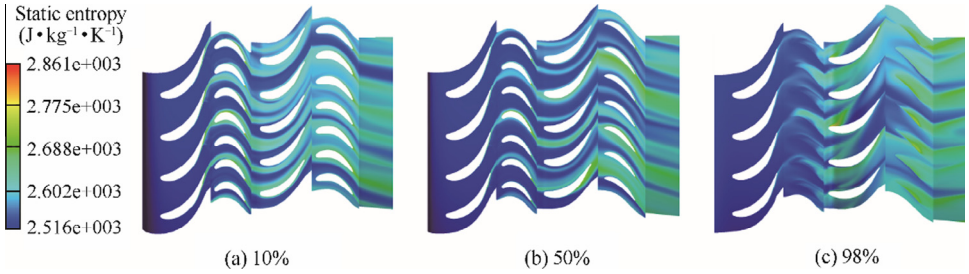

Fig. 14 Static entropy at different spans.

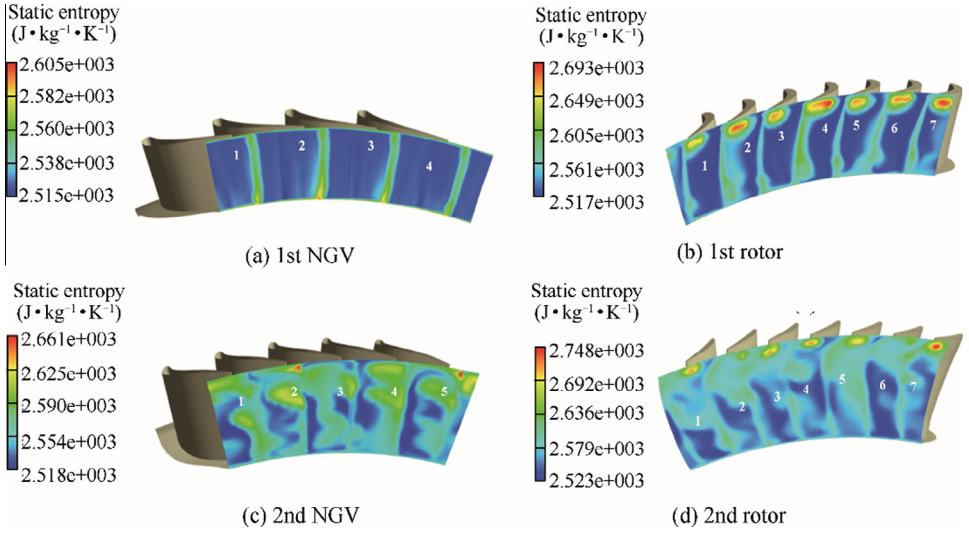

Fig. 15 Static entropy at exit from components.

secondary flows at the hub corner as well as a vortex structure seen at the tip of blades. As well illustrated, the hub corner secondary flow is more important in the 2nd, 4th and 6th blades, whereas the tip vortices are more important for the 2nd, 4th, 6th and 7th blades. The wakes generated by first NGV are seen to envelop completely 2nd 4th and 6th blades, but on the contrary they are far away from 1st, 3rd and 5th blades. At exit of second NGV, the entropy contours (Fig. 15(c)) illustrate accentuated flow distortions resulting from flow maldistributions convected from first rotor. The highest level of entropy is seen behind the second rotor blades (Fig. 15(d)) owing to cumulated wakes and flow distortions originated from upstream components. The intensity of tip vortex seems to be affected by the relative position between vanes and blades of the second stage. As revealed for 2nd and 6th blades, the size of tip vortex is smaller compared to other blades. At 10% and 90% spans of first rotor blade, the secondary flows and tip vortex flows mix with upstream wakes so that the entropy into the second NGV is spread uniformly. The blade tip vortex strikes the downstream vane leading edge and displaces to the pressure side of the upper part. As a consequence of the viscous effects, significant losses are generated by the tip leakage flow in regions inside and outside the blade tip gap. The mixing process between the leakage flow and the mainstream flow is responsible for additional entropy creation.

Although the use of one vane/blade per a component seems to be sufficient in predicting the average expansion properties and the subsequent performance maps of the stages of an axial turbine, but is rather enable to reveal the real physics of interactions between the successive vane and blade rows. In the other side, the use of multi-blade per a component and the scaling technique in order to keep the true periodicity better revealed the effects of relative positions between vanes and blades on the flow structures, characterized by distortions especially the second stage.

4. Unsteady flow simulations

The computations of transient flows were carried out based on the transient rotor/stator interface to account for the vane/rotor interactions, where the relative motion is considered via the general grid interface (GGI) connection. This latter allows connecting grids of non-matching surface extent, nodes locations and elements types. The unsteady computations used the second order transient scheme for the transient term discretization. The time step was taken small enough to get the necessary time resolution depending on the rotational speed of the turbine. The transient simulations consist in physically advancing the flow in a real time, and because of unsteady flow it is not possible to use the final time-step's flow field alone in order to assess the convergence in terms of RMS/MAX residuals and imbalances, but some sort of average over an appropriate timescale is required. Therefore, it is necessary to get the individual time-steps to converge and also small enough as afforded by the computing resources. The residual was set equal to 10–6, and the solver iterates till a number of 100 times per a step, and if this criterion is not met, the residual line goes straight with the next iteration. So, this usually requires a smaller time step and would take too much time to finish one cycle. The total time of simulation corresponded to one round of the rotor which is equal to 5.6872 ms. The inner time step corresponded to $\Delta t = 7.8989$ μs equivalent to 0.5 deg of the first blade row. This sampling time step was taken to have a good accuracy within the afforded computing resources. The results of the steady frozen rotor simulations were used to initialize the transient simulations.

4.1. Spectral analysis

Fast and simple analysis based on FFT is done for the static pressure fluctuations recorded at different points and lines of the interfaces planes. The obtained spectrums provided helpful information in identifying the prevailing modes and the sources of the cyclic fluctuations, since every source or structure is characterized by its modal frequency. In addition, such an analysis may provide information about the locations of the probes during experiments. The interaction phenomena produced by the displacement of rotating blades against stationary vanes are defined in the chorochronic periodicity model by a superposition of infinity of rotating waves.[23] This model originates from the fact that the flow is characterized by a double periodicity (space and time) as explained by Gerolymos et al.[8] When two blade rows in a relative angular motion are considered, the unsteady flow in the frame of reference rotating is periodic and its fundamental frequency is the rotor blade passing frequency BPF. When one blade row is considered, the spatial periodicity is equal to the pitch range, but for two rows

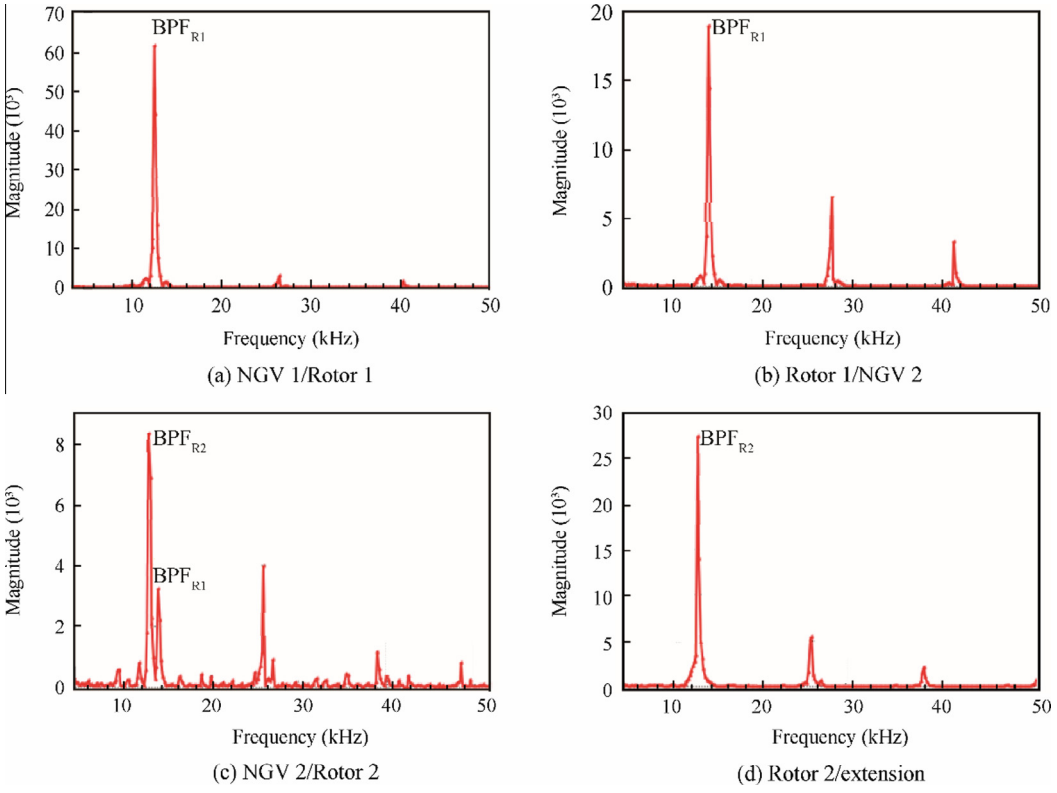

Fig. 16 FFT spectrums of pressure signals recorded half way at mid-span (nominal operating point).

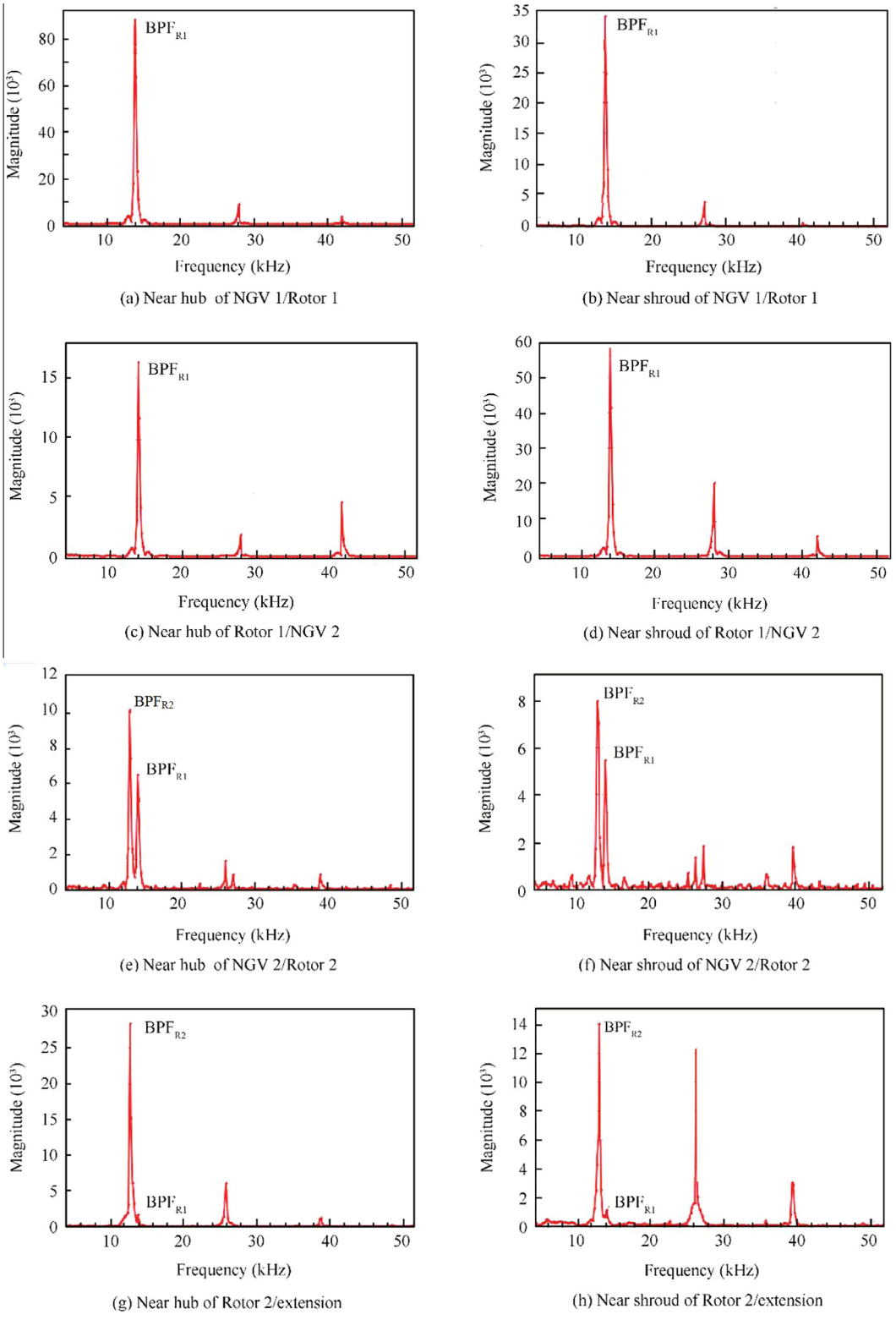

Fig. 17 FFT spectrums of pressure signals recorded half way near hub and shroud (nominal operating point).

with different blades counts, the unique spatial periodicity corresponds to 2π. A particular case exists if blades counts are multiples of a number N where the spatial periodicity is equal to $(2\pi/N)$. These periodicities imply that each flow property is invariable by the spatial or temporal transformation as highlighted by Miton et al.[24] If the aerodynamic instabilities are neglected, the unsteady flow in a frame rotating with a given row is periodic with a fundamental frequency BPF of the adjacent blade row.

$$\begin{cases} f_1 = (N_{R2}/2\pi)|\Omega_1 - \Omega_2| \\ f_2 = (N_{R1}/2\pi)|\Omega_1 - \Omega_2| \end{cases} \quad (1)$$

Ω_1 and Ω_2 are the speed of rotation of rotor 1 and 2. N_{R1} and N_{R2} are the blade count of rotor 1 and 2.

When the flow around two neighboring blades of a given row is considered, each blade witnesses the same phenomenon as its neighbor, but with a phase shift β which is a simple function of blades counts and the direction of relative rotation.

$$\begin{cases} \beta_1 = 2\pi \frac{N_{R1}-N_{R2}}{N_{R1}} sign[\Omega_1 - \Omega_2] \\ \beta_2 = -2\pi \frac{N_{R2}-N_{R1}}{N_{R2}} sign[\Omega_2 - \Omega_1] \end{cases} \quad (2)$$

So the chorochronic periodicity for the property of static pressure for the blade row 1 or 2 can be expressed by

$$p_i(r,\theta_i,z,t) = p_i\left(r,\theta_i - \frac{2\pi}{N_{Ri}}, z, t + \frac{\beta_i}{2\pi f_i}\right), \quad i = 1,2 \quad (3)$$

where r is the radial coordinate, θ_i is the tangential coordinate, f_i is the fundamental frequency and β_i is the phase shift. Subscript i stands for rotor 1 or 2.

Because of the double periodicity in time and space, it is natural to express the pressure signal in each frame of reference by a double, time t and space θ, Fourier series:

$$p(r,\theta_i,z,t) = \sum_{n-\infty}^{+\infty} \sum_{m-\infty}^{+\infty} P_{mn}(z,r) e^{i[m\theta - nN_{Ri}\Omega_i t + \phi_{mn}]} \quad (4)$$

The sum over n represents the time harmonics and that over m the space harmonics. $P_{mn}(r,z)$, $\phi_{m,n}$ are the amplitude and the phase at a given position. The above sum is modeled as a superposition of infinity of rotating waves; each is characterized by phase and amplitude, and the rotating speed Ω_m depends on the blade row rotational speed as below.

$$\Omega_{mi} = \frac{nN_{Ri}}{m}\Omega_i \quad (5)$$

Teyler and Sofrin[23] in their theory provided a relation, as below, between the time mode and the space mode, where N_R et N_S are the rotor and stator blade counts:

$$m = nN_R + kN_S \quad k = ..,-1,0,1,\ldots \quad (6)$$

The analysis of interactions phenomena is reduced to few parameters such as the amplitude and rotational speed. It is hard to observe the chorochronic periodicity in the time domain, and this is why FFT analysis is performed for the static pressure fluctuations to identify their different frequencies and evolutions in time (domination, appearance or disappearance). Moreover, FFT analysis of pressure signals allows determining the different existing modes and highlights the most dominant ones as well as the speed of the corresponding rotating wave.

4.2. One-blade per passage simulations

The transient rotor/stator interface and the second order transient scheme were used. The local time step was set equivalent to 0.5 deg to get the necessary time resolution, and for one round of the turbine the total simulation time is equal to 5.687 ms. At each interface, the temporal pressure signals were recorded at mid-pitch points located at 10% span, mid-span and 98% span. The temporal signals of static pressure depict a fluctuating character related to the rotation of blades. Spectrums of static pressure fluctuations recorded at mid-span of first and second interfaces (Fig. 16) exhibit principal peaks of frequencies corresponding to the first rotor $BPF_{R1} = \frac{\Omega}{60} N_{R1} = 14.06$ kHz. For the third interface there is a dominant peak corresponding to the second rotor $BPF_{R2} = \frac{\Omega}{60} N_{R2} = 13.01$ kHz, in addition to another peak corresponding to BPF_{R1}. At the fourth interface the principal peak is at a frequency which is related to BPF_{R2}. The other observed peaks of lower amplitudes may be attributed to the turbulent structures generated behind blades. As a conclusion, FFT analysis revealed emergence of pressure waves related to the potential effect propagating both upstream and downstream of moving blades and disturbing the flow structure through the successive passages.

FFT spectrums of temporal pressure fluctuations recorded near the hub (Fig. 17) exhibit important fluctuations as the flow is affected by the wake and passage vortex behind the first NGV. At the second interface, the amplitude of temporal pressure fluctuations is more important near shroud than hub due to tip leakage vortex accentuating the flow perturbations behind the first rotor blade. The second harmonic that corresponds to the second rotor blade passing frequency BPF_{R2} is more because of the tip leakage flow acting as a second disturbance within each blade passing period. For the third interface (NGV2/rotor2), the pressure fluctuation has a similar structure along the spanwise direction which is composed at least by two waves as revealed by the two principal peaks of BPF_{R2} and BPF_{R1} (equal to 13.01 kHz and 14.06 kHz, respectively). The attenuation of static pressure fluctuations at 90% span may be explained by the interaction of upstream thick boundary layer and tip leakage flow. The fourth interface (rotor2/extension) is characterized by a fluctuation near the hub which is stronger than that at shroud and indicated by the fundamental frequencies BPF_{R2} and BPF_{R1}. According to the spectrums in Fig. 17(g) and (h) the pressure wave generated by the first rotor blades is shown to decay in amplitude. The blade tip vortex seems to have a strong interaction with the downstream NGV even with the considerable axial spacing between them. Beyond 90% span, the unsteady pressure is significantly influenced by the tip-clearance flow and indicates that the blade tip-vortex flow does not mix enough as it is convected along the endwall.

After an elapsed time of 5.624 ms which corresponds to the blades positions indicated by Fig. 18, the spatial pressure signals were recorded over lines at 10% span, mid-span and 98% span of each interface plane. At mid-span, the spatial pressure fluctuations (Fig. 19) exhibit an almost periodic character with a repeating trend over the circumferential direction. For interface NGV1/rotor1, the related spectrum reveals a harmonic of 78.79 and its multiples close to the first rotor blade

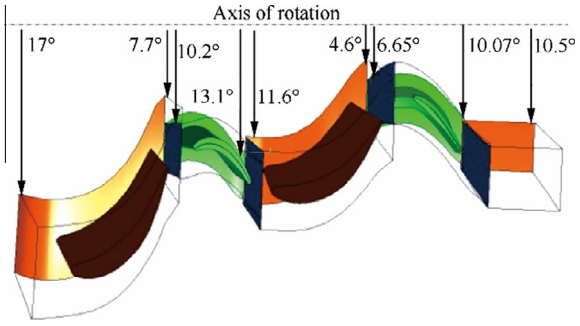

Fig. 18 Angular positions at a period of time of 5.624 ms.

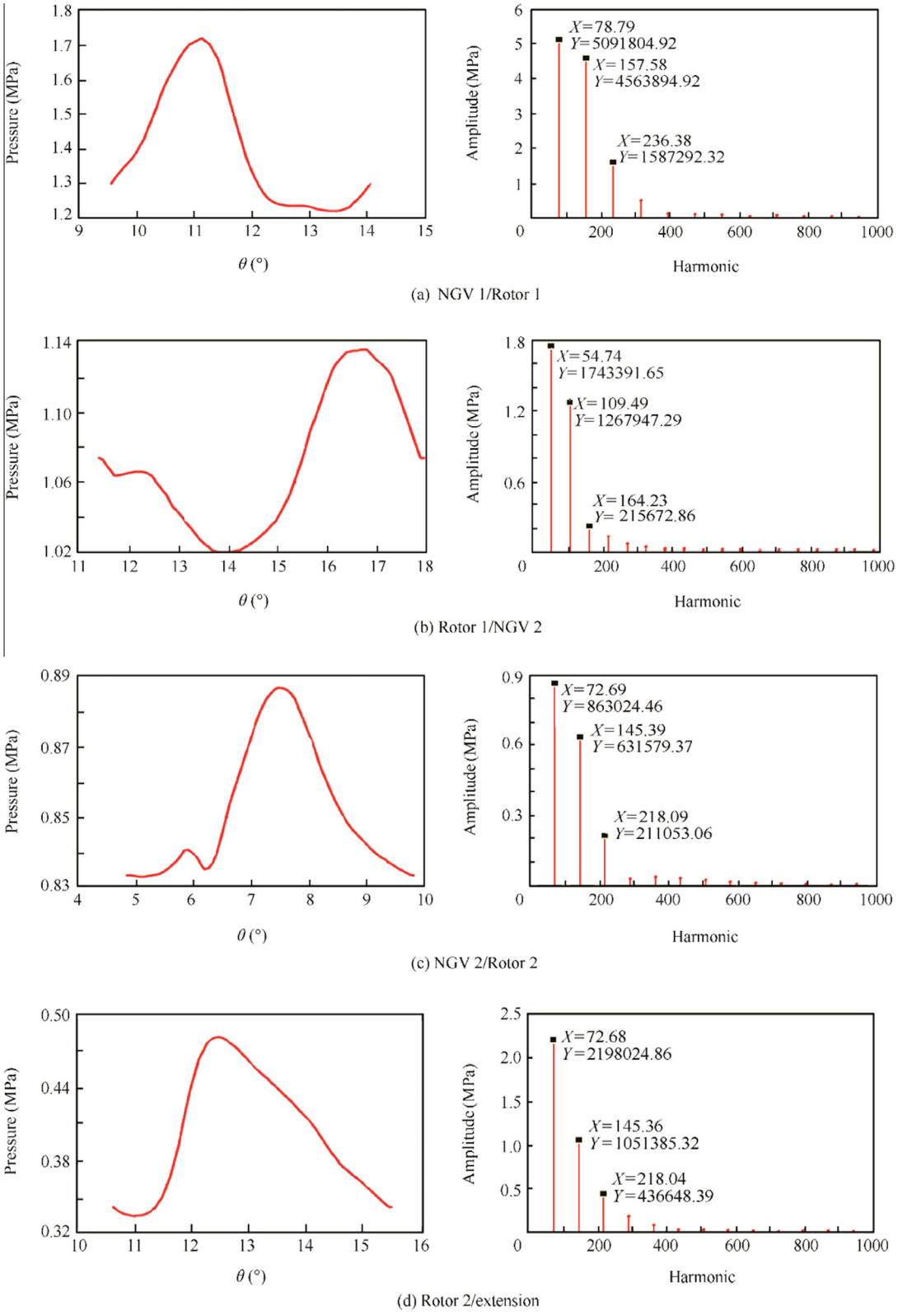

Fig. 19 FFT spectrums of spatial pressure fluctuations recorded along circumferential lines at mid-span (nominal operating point).

count. At interface rotor1/NGV2 the dominant harmonic is equal to 54.74, close to the second NGV vane count. Finally, for the interfaces NGV2/rotor2 and rotor2/extension, the main harmonics are equal to 72.69 and 72.68 which are close to the second rotor blade count. The spatial pressure fluctuations recorded along circumferential lines near the hub exhibit

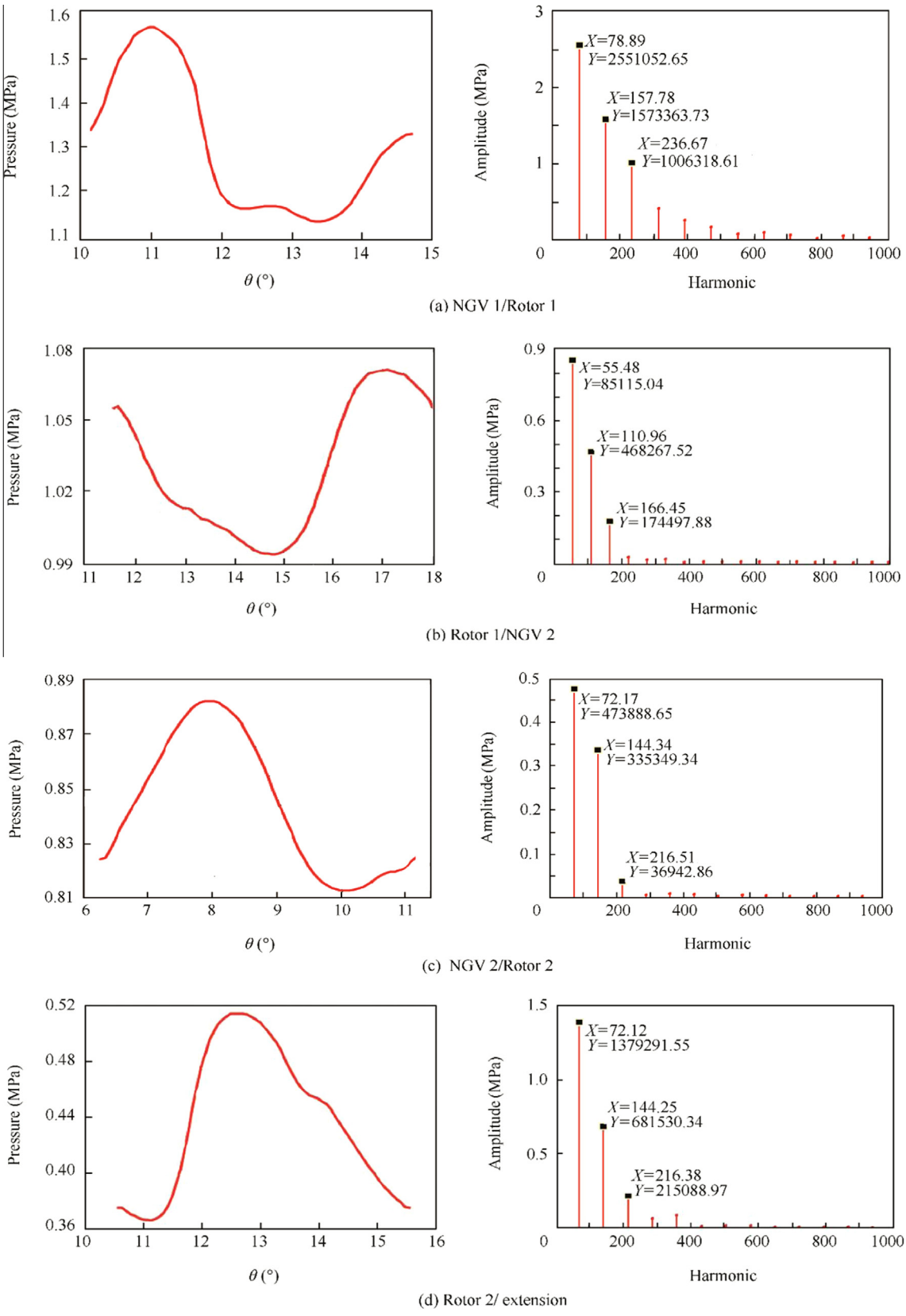

Fig. 20 FFT spectrums of spatial pressure fluctuations recorded along circumferential lines near hub (nominal operating point).

(Fig. 20) almost similar trends as at mid-span, but there are differences due to the variations of relative angular positions between successive vanes and blades rows. The dominant harmonics are those corresponding to the blade count of the component downstream of an interface. The angular shift characterizing each spatial fluctuation corresponds to the posi-

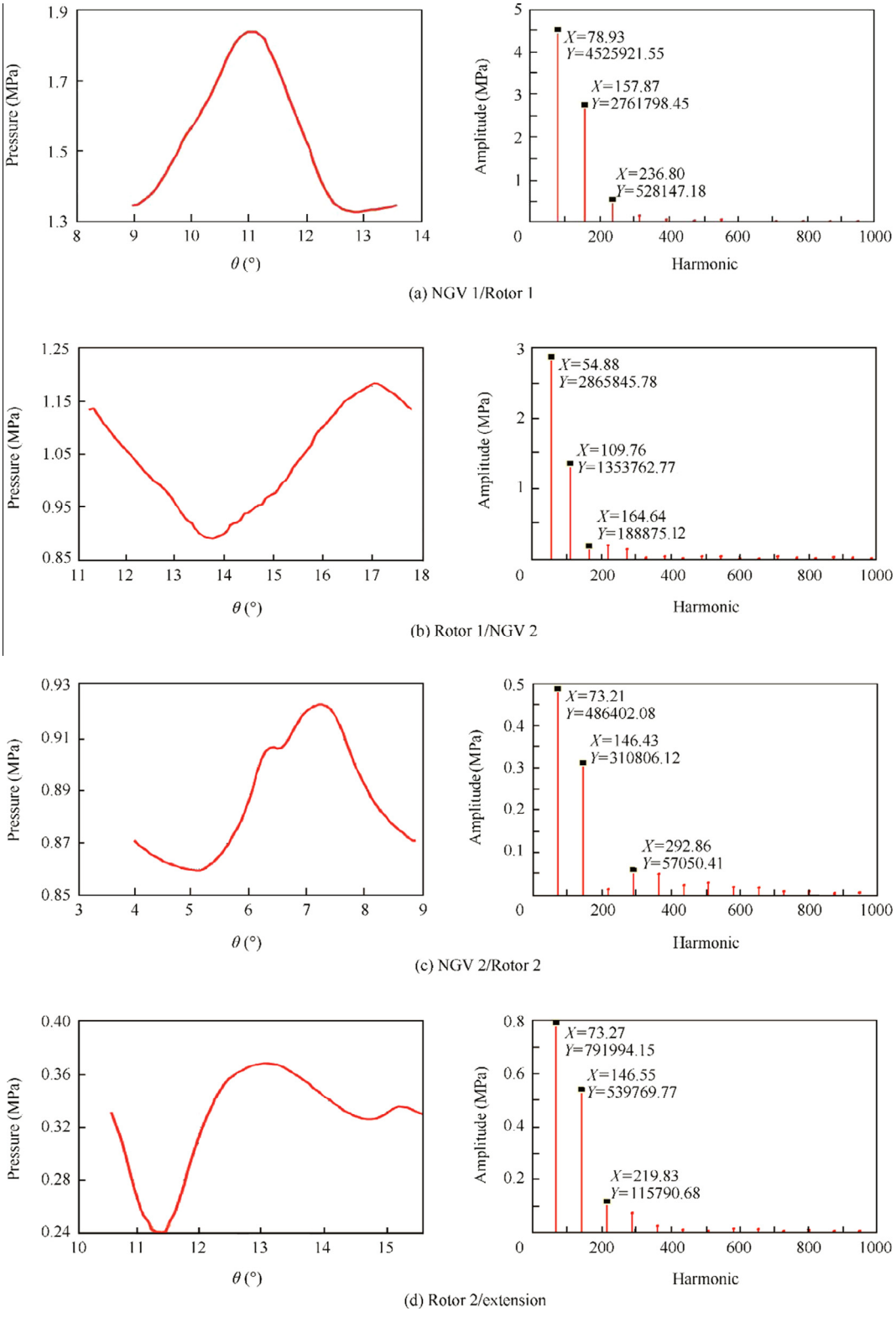

Fig. 21 FFT spectrums of spatial pressure fluctuations recorded along circumferential lines near shroud (nominal operating point).

tion of the downstream component at this instant. For the interfaces rotor1/NGV2 and rotor2/extension, the spatial pressure fluctuations recorded along circumferential lines near the shroud (Fig. 21) exhibit larger perturbations and flow distortions induced by leakage flow and tip vortices. The wave structure exhibits a number of lobes equal to the blade count of each row, for which the harmonics and the rotational speed of first and second rotor are calculated from Eqs. (5) and (6). For instance, to have the mode $m = 80$, the values $n = 1$ and $k = 0$ are taken; leading to a rotational speed Ω_{m1} equal to

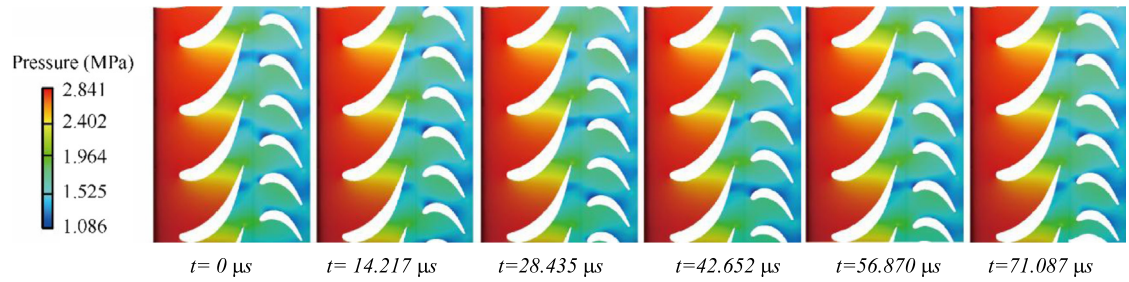

Fig. 22 Unsteady pressure at mid-span of multi-blade passages, case of NGV1/rotor1 interactions.

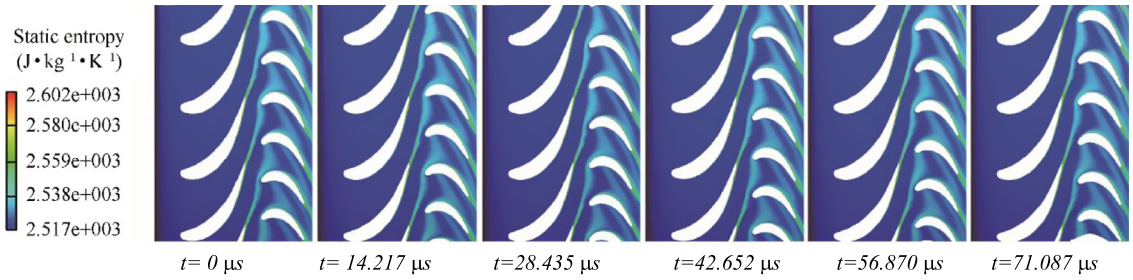

Fig. 23 Unsteady entropy at mid-span of multi-blade passages, case of NGV1/rotor1 interactions.

10,550 rpm. These modes are unique and represent the potential effect of rotor blades propagating both upstream and downstream. At a very low mass flow rate, the spectrums of temporal pressure signals recorded at the interfaces NGV2/rotor2 and rotor2/extension exhibit peaks of frequencies of low amplitudes corresponding to BPF_{R1}, revealing a propagating pressure wave generated by the first rotor through the second rotor, as well as a decaying amplitude due to the dumping effect. Except for the interface rotor1/NGV2, the dominant frequencies BPF_{R1} and BPF_{R2} are more important near hub than at mid-span, which may be related to the high flow disturbances convected downstream of blade rows. Near the shroud the spectrums reveal secondary peaks at interfaces NGV2/rotor2 and rotor2/extension corresponding to the vortex structures occurring through the second blade row. The passage vortex and leakage vortex interacting with the tip horseshoe vortex of the second rotor lead to more flow perturbations near the casing. On the contrary, the pressure wave generated by the first rotor blade is the dominant perturbation characterized by peaks of frequency corresponding to BPF_{R1} = 14.06 - kHz. For the two other interfaces, the pressure signals recorded near the hub of each component have almost similar trends as those at mid-span, whereas for the interfaces NGV2/rotor2 and rotor2/extension, the pressure signals differ due to flow distortions induced by the hub corner vortex structure. Near the shroud, the spectrums relate the distortions due to leakage flow and tip vortices downstream of first rotor and the next component. FFT spectrums reveal first harmonic corresponding to the blade count of upstream component. Moreover, at interface rotor2/extension, the dominant harmonic m = 219.83 (corresponding to 74 × 3 = 222) is obtained by setting n = 1 and k = 2, and subsequently the rotational speed Ω_{m2} is equal to 3516.66 rpm.

The flow simulations based on a one-blade per component seem to under-evaluate and hide details of unsteadiness related to the effect of relative positions between rotating blades and stationary vanes, particularly the transport of wakes which interact with the secondary flows and affect the development of tip vortices. Furthermore, the spatial modulation of flows through the components does not lead to the correct parameters of chorochronic periodicity characterizing the stator/rotor interactions. Indeed, these simulations may only produce results for the temporal variations of flows properties characterized by periodic fluctuations related to the rotating blades and known as the potential effect that propagates both upstream and downstream of components.

4.3. Multi-blade per passage simulations

Unsteady flow simulations based on multi-blade per passage used the transient rotor/stator interface and started from the frozen-rotor steady flow results. Fig. 22 presents a succession of images illustrating the instantaneous pressure distributions at mid-span of NGV1 and rotor1, corresponding to five time steps of 71.087 μs (each time step is 14.217 μs) covering one blade passing pitch. As well illustrated, the static pressure distributions in the first rotor exhibit a non-regular depression zone over the blades which are repeated after an elapsed time equal to the rotor blade passing period, i.e. the patterns between the starting time and the time of 71.087 μs are practically similar. Moreover, these patterns occur with a phase shift equal to the pitch of first NGV. According to these patterns, it may be concluded that the applicability of the chorochronic periodicity is well illustrated with multi-blade per component.

The generated entropy due to NGV1/rotor1 interactions during one rotor blade passing period is well illustrated by Fig. 23, revealing additional losses in the unsteady transport of wakes through the downstream blade row. The wakes formed by the first NGV are chopped by the first rotor blades and transported further beyond the trailing edges where they

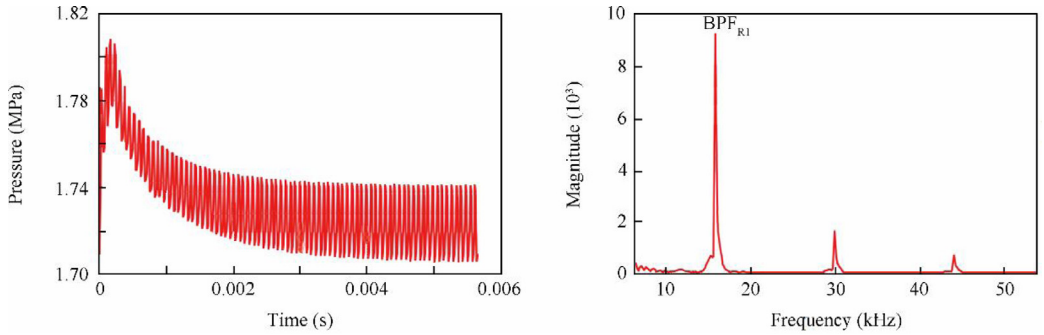

(a) NGV1/Rotor1 (mid-span)

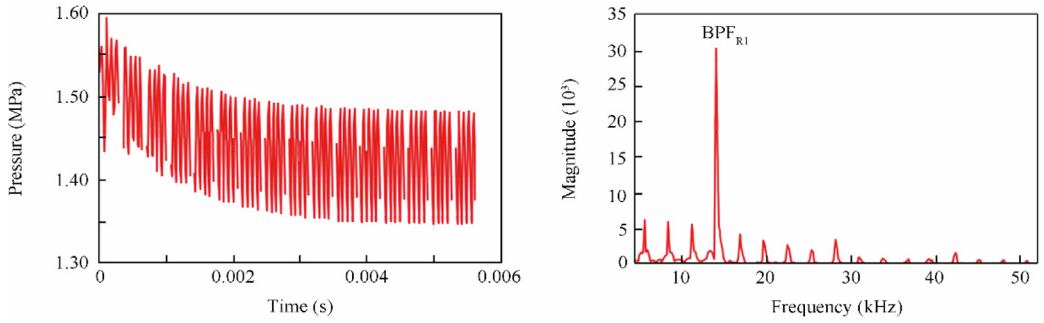

(b) Rotor1/NGV2 (mid-span)

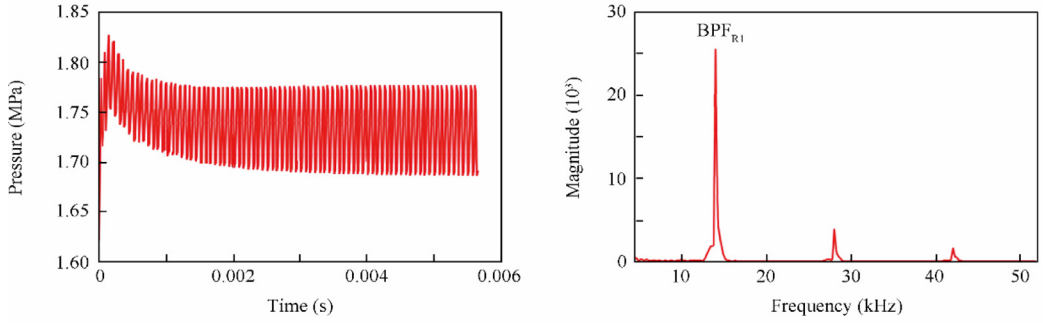

(c) NGV1/Rotor1 (near hub)

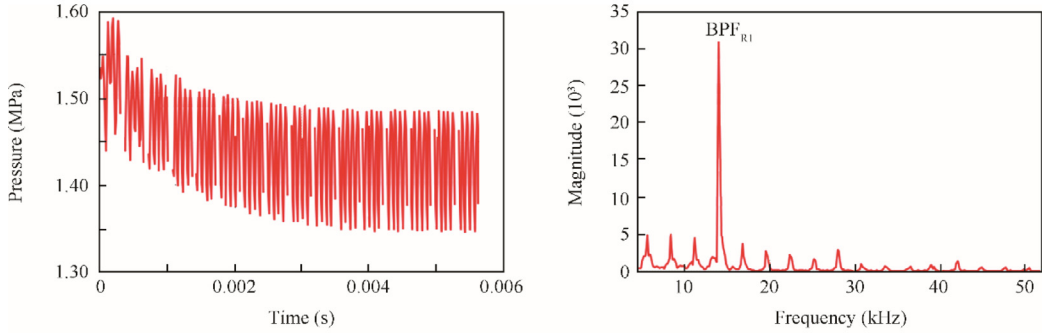

(d) Rotor1/NGV2 (near hub)

Fig. 24 Temporal pressure fluctuations and FFT spectrums, recording at half-pitch at interfaces NGV1/rotor1 and rotor1/NGV2.

interact with the wakes, hence resulting in intensified aerodynamic losses and flow distortions towards the second stage. The transport of NGV wakes leads to significant fluctuations in the sizes of secondary flows and separation from blade suction side can be explained by the local changes of inlet flow angle during the time of interactions with the passing wakes.

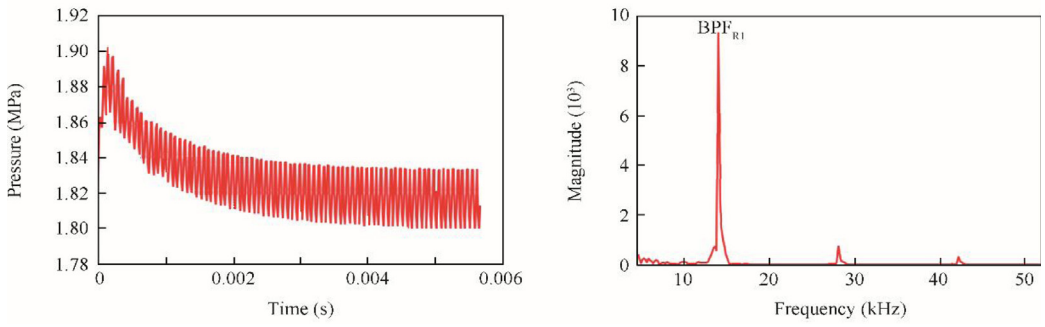

(e) NGV1/Rotor1 (near shroud)

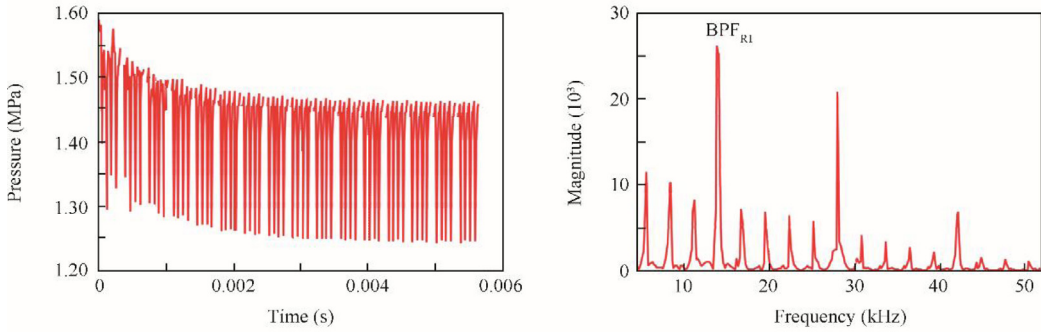

(f) Rotor1/NGV2 (near shroud)

Fig. 24 (*continued*)

The kinetic energy of the tip leakage vortex is in a large part dissipated during its transport in the structure of the vane passage vortex.

The temporal static pressure fluctuations recorded at mid-pitch of interfaces NGV1/rotor1 and rotor1/NGV2 reveal a transitory mode wherein the static pressure reaches a peaked value, and then after a period of time about 4 ms it decreases towards a plateau modulated by periodic fluctuations. The subsequent spectrums illustrated by Fig. 24(a) and (b) exhibit a principal peak at BPF_{R1} = 14.06 kHz corresponding to a pressure wave propagating both upstream and downstream of blades rows, and also reveal secondary peaks related to flow perturbations downstream of the rotor blades. The temporal pressure fluctuations recorded at half-pitch near the hub of interfaces NGV1/rotor1 and rotor1/NGV2 reveal a transitory mode more important than that at mid-span for first interface, but on the contrary for the second interface the amplitudes of fluctuations are mostly alike. The perturbations generated near the hub seem to extend till mid-span downstream of first rotor, as confirmed by the spectrums of Fig. 24(c) and (d) which depict a dominant BPF_{R1} near the hub for interface NGV1/rotor1, whereas for interface rotor1/NGV2 the amplitudes are practically the same. Near the shroud of interface NGV1/rotor1 (Fig. 24(e)) the amplitudes of pressure fluctuations differ due to important flow perturbations which are even higher for interface rotor1/NGV2 (Fig. 24(f)) as related to the tip leakage flow and vortices.

The spatial distributions of static pressure recorded, after an instant of 5.687 ms, along circumferential lines passing at mid-span of interfaces NGV1/rotor1 and rotor1/NGV2 are presented through Fig. 25(a) and (b). At first interface there is a, evidence of regular pressure fluctuations between over-pressure to under-pressure, but on the contrary for the second interface the fluctuations do not behave the same due to relative positions between the trailing edges of first NGV and the leading edges of first rotor blades. FFT analysis reveals harmonics multiple of 12 because the large spatial periodicity is equal to $2\pi/12$. At interface NGV1/rotor1, the lobed structure generated by first NGV has a dominant harmonic m = 47.83 related to the vane count, whereas at interface rotor1/NGV2 there is a dominant harmonic m = 32 which is a combination between the first vane count and first rotor blade count (Eq. (6)). The frequency BPF_{R1} = 14.06 kHz detected downstream of first rotor corresponds to the time harmonic n = 1, and in order to get the spatial mode m = 32, the value of k = −1 has to be taken. Fig. 25(c) and (d) present the spatial distributions of static pressure recorded along lines passing near the hub. The corresponding spectrums reveal a dominant harmonic m = 32 arising from the interaction between first NGV and first rotor blade, and the speed of this lobed structure Ω_{m1} = 26,375 rpm which is the same as that at mid-span. The spectrums (Fig. 25(e) and (f)) related to the spatial pressure distributions recorded along lines passing near shroud reveal that the potential effect due to first NGV characterized by the harmonic m = 47.67 (first vane count) prevails along the totality of blade span. At interface rotor1/NGV2 the spectrum depicts (Fig. 25(f)) a dominant harmonic m = 79.22 that corresponds to first rotor blade count, in addition to other peaks which might be related to the blade passage vortex, tip leakage flow and tip vortices.

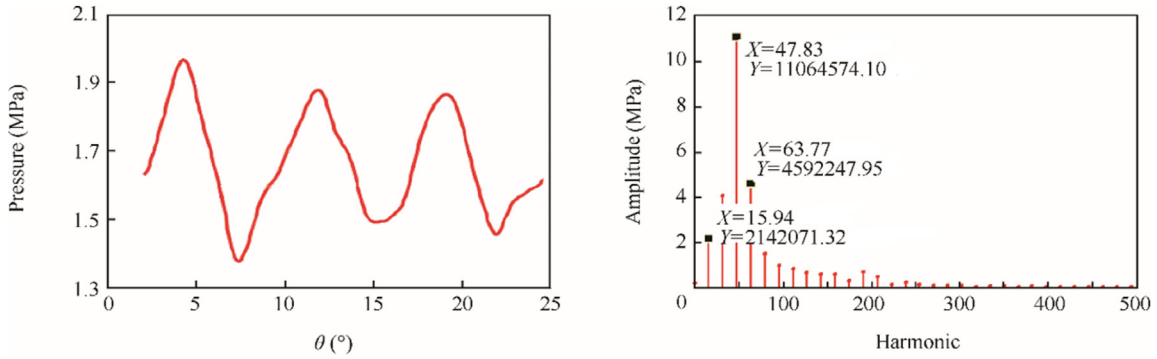

(a) NGV1/Rotor1 (mid-span)

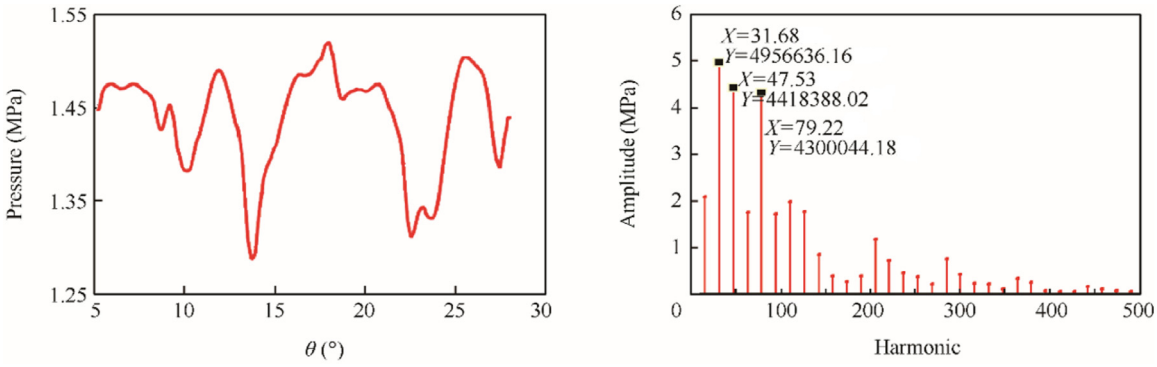

(b) Rotor1/NGV2 (mid-span)

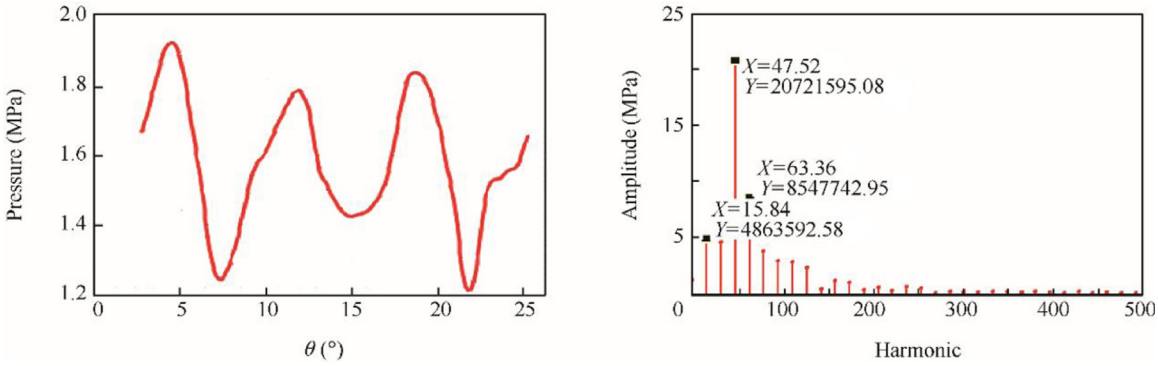

(c) NGV1/Rotor1 (near hub)

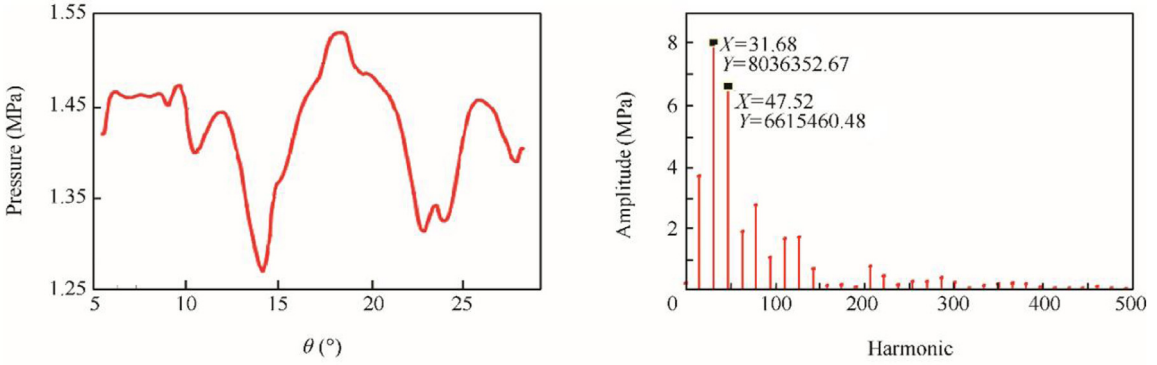

(d) Rotor1/NGV2 (near hub)

Fig. 25 Spatial pressure fluctuations and FFT spectrums, recording along lines near hub and shroud at interfaces NGV1/rotor1 and rotor1/NGV2.

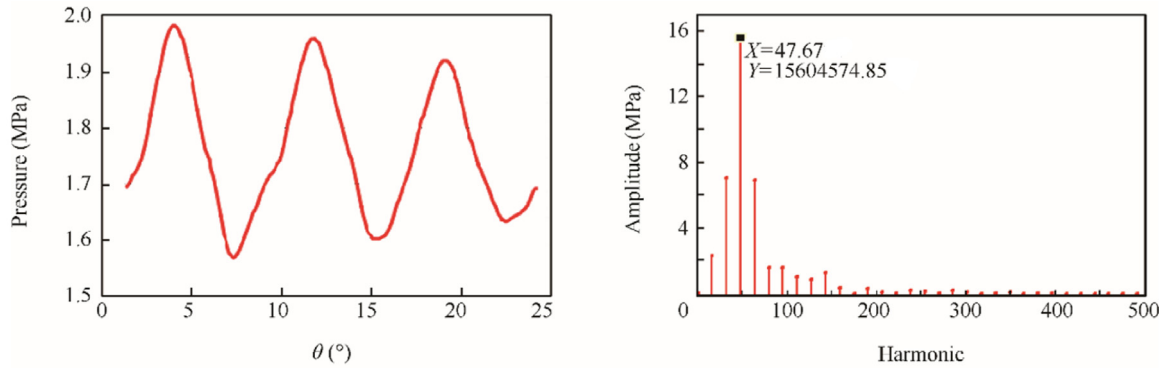

(e) NGV1/Rotor1 (near shroud)

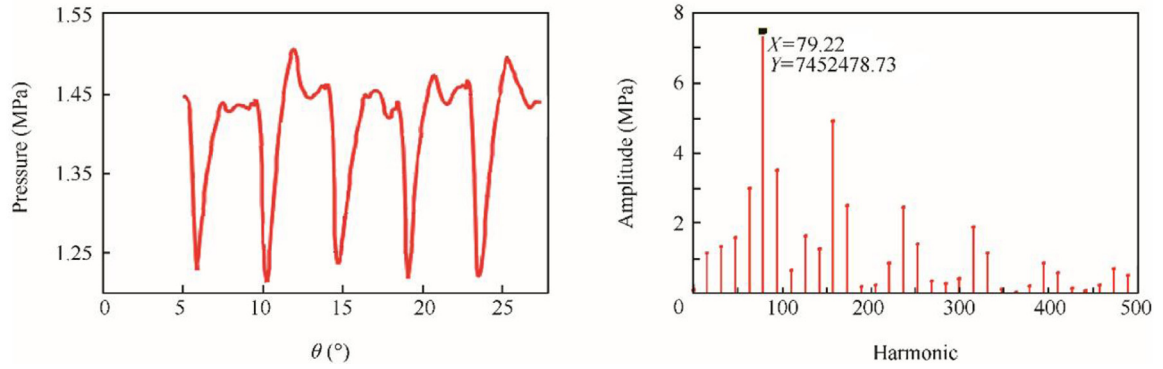

(f) Rotor1/NGV2 (near shroud)

Fig. 25 (*continued*)

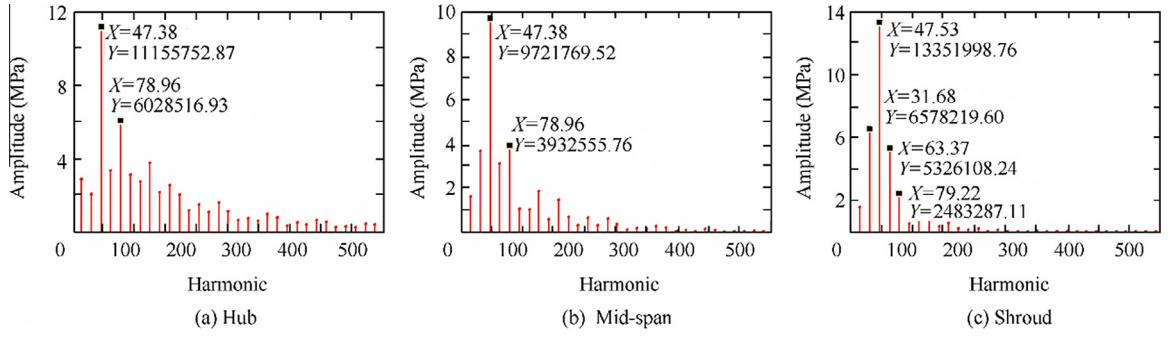

Fig. 26 FFT spectrums of static pressure recoded near leading edge of first rotor blade.

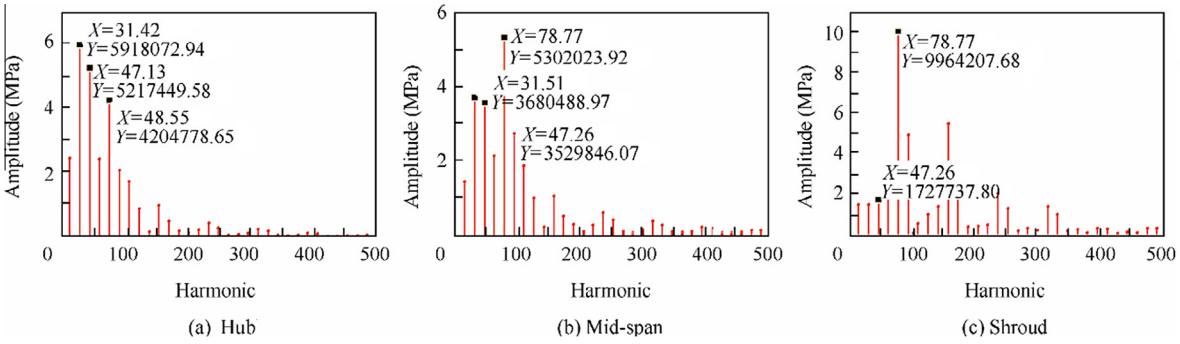

Fig. 27 FFT spectrums of static pressure recoded behind trailing edge of first rotor blade.

The spatial distributions of static pressure recorded along circumferential lines passing near the leading edge of first rotor blades and their respective spectrums (Fig. 26(a)–(c)) depict clearly the propagating wave phenomenon related to the potential effect attributed to first NGV. The harmonics close to the value of 80 seem to have higher amplitudes compared to those of the first interface, hence revealing the importance of the first rotor potential effect. Just behind the first rotor blades (Fig. 27(a)–(c)), FFT analysis reveals a harmonic of 31.42 representative of the mode of interaction NGV1/rotor1 near the hub, which is more dominant as compared to potential effects of first NGV and rotor characterized by harmonics 47.13 and 78.55, successively. At mid-span, the potential effect related to first rotor is more important compared to that due to first NGV. Near shroud, the interaction of NGV1/rotor1 is revealed by the harmonic 96 which is a combination of $n = 3$ and $k = 3$, leading to a pressure wave rotating at a speed $\Omega_{m1} = 26{,}375$ rpm. The region of high pressure unsteadiness located at the upper of leading edge from suction side is due to interactions of vanes with the blade, typically the vanes wakes with blade tip-vortices. Another region of high unsteadiness located at the second vane leading edge above 90% span is attributed to blade tip vortices convected inboard through the transition duct.

The simulations of unsteady flows of an hp two-stage axial turbine based on the scaled multi-blade passages allowed predicting other spatial harmonics which were not detected from one-blade passage simulations which only permitted detecting harmonics related to vane and blade counts. Downstream of first rotor, the effects of interactions are seen to be dominant from hub to mid-span; while near the shroud the dominant harmonics correspond to the additional effects of tip leakage flow and tip vortices.

5. Conclusions

The predicted performance maps of this two-stage axial turbine depict that the aerodynamic characteristics of first stage are independent from the second stage, but on the contrary, the second stage is strongly influenced by the first stage. The multi-blade per passage and the scaling technique allowed investigating the flow details and the effects of relative motion between vanes and blades. The wakes generated from upstream components are shown to induce circumferential distortions and interact with the secondary flows and tip leakage flow and vortices of next blade row, thus leading to more entropy generation.

FFT analysis revealed high flow unsteadiness which was characterized by a space–time periodicity and described by a double Fourier decomposition, hence leading to the determination of different frequencies and prevailing modes and their originating sources. The circumferential distributions of static pressure at each interface show a lobed structure of pressure wave corresponding to the vane and blade counts propagating both upstream and downstream of the components. The potential effect is seen to prevail along the quasi totality of blade span, while downstream of blades and near the shroud the dominant effect is rather attributed to the tip flow vortical structure. Finally, this study produced an insight about some complex phenomena related to vanes/blades interactions, and also may guide experimentalists to set the effective positions for the pressure probes positions in order to get the complete measurements data.

References

1. Dawes N. Towards improved through flow capability: the use of 3d viscous flow solvers in a multistage environment. *ASME J Turbomach* 1992;**114**(1):8–17.
2. Deiter B, Jing R. *Influence of stator clocking on the unsteady three-dimensional flow in a two-stage turbine. ASME Paper GT2004-53511*, 2004.
3. Erdos J, Alznerf E, McNally W. Numerical solution of periodic transonic flow through a fan stage. *AIAA J* 1977;**15**(11):1559–68.
4. Adamczyk JJ. Model equation of simulating flows in multistage turbomachinery. *ASME J Turbomach* 1985;**85**:226–39.
5. Adamczyk JJ, Celectina ML, Beach TA, Bernett M. Simulation of 3d viscous flow within a multistage turbine. *ASME J Turbomach* 2010;**110**(12):370–6.
6. Giles M. Calculation of unsteady wake/rotor interaction. *AIAA J Propul Power* 1988;**4**(4):356–62.
7. Lebrun M, Favre C. *Fan-OGV unsteady Navier–Stokes computation using an adapted acoustic mesh. Paper No. AIAA-2004-2995*. Reston: AIAA; 2004.
8. Gerolymos GA, Michon GJ, Neubauer J. Analysis and application of chorochronic periodicity in turbomachinery rotor/stator interaction computations. *AIAA J Propul Power* 2002;**18**(6):1139–52.
9. Miller RJ, Moss RW, Ainsworth RW, Harvey NW. Time resolved vane-rotor-vane interaction in a transonic one and a half stage turbine. *Proc Inst Mech Eng Part A* 2001;**215**(5):675–85.
10. Miller RJ, Moss RW, Ainsworth RW, Harvey NW. Wake, shock, and potential field interactions in a 1.5 stage turbine – Part I: Vane-rotor and rotor-vane interaction". *ASME J Turbomach* 2003;**125**(1):33–9.
11. Rai M, Madavan N. Multi-airfoil Navier–Stokes simulations of turbine rotor/stator interaction. *ASME J Turbomach* 1990;**112**(3):377–84.
12. Arnone A, Pacciani R. Rotor-stator interaction analysis using the Navier–stokes equations and a multi-grid method. *ASME J Turbomach* 1996;**118**(4):679–89.
13. Clark JP, Stetson GM, Magge SS, Ni RH, Haldeman CW, Dunn MG. *The effect of airfoil scaling on the predicted unsteady loading on the blade of a 1 and 1/2 stage transonic turbine and a comparison with experimental results. ASME Paper 2000-GT-0446*, 2000.
14. Yao J, Davis R, Alonso J, Jameson A. Massively parallel simulation of the unsteady flow in an axial turbine stage. *AIAA J Propul Power* 2002;**18**(2):465–71.
15. He L, Chen T. Analysis of rotor-stator and stator-rotor interferences in multi-stage turbomachines. *ASME J Turbomach* 2002;**124**(4):564–71.
16. Hodson HP. Measurements of wake generated unsteadiness in the rotor passages of axial flow turbine. *ASME J Eng Gas Turbines Power* 1985;**107**(2):467–76.
17. Sharma OP, Renaud E, Butler TL, Milsaps K, Dring RP, Joslyn HD. *Rotor–stator interaction in multistage axial flow turbines. Reston: AIAA Paper: AIAA-1988-3013*, 1988.
18. Walraevens RE, Gallus HE, Jung AR, Mayer JF, Stetter H. *Experimental and computational study of the unsteady flow in a 1.5 stage axial turbine with emphasis on the secondary flow in the second stator. ASME Paper 1998-GT-254*, 1998.
19. Behr T, Kalfas A, Abhari RS. *Unsteady flow physics and performance of a one-and-1/2-stage unshrouded high work turbine. ASME Paper GT-2006-90959*, 2006.
20. Qi L, Zhou YP. Turbine blade tip leakage flow control by unsteady periodic wakes of upstream blade row. *Procedia Eng* 2014;**80**:202–15.

21. CFX-Solver Theory Guide. *Ansys-CFX Release 12.0*, 2009, Canonsburg, USA.
22. CF6-80 student notebook, GEK 50485, Aircraft Engine Business Group, Cincinnati, General Electric Company, Ohio 45215–6301, Edition 6–IM, June 1, 1983.
23. Tyler JM, Sofrin TG. Axial flow compressor noise studies. *SAE Trans* 1962;**70**:309–32.
24. Miton H, Belhabib M, Kus U. Experimental and numerical investigation of unsteady flow properties in a stator of multistage axial flow compressor*Lecture in AGARD Conference Proceedings 571, Losses Mechanisms and Unsteady Flows in Turbomachines, Propulsion and Energetics Panel (PEP), 85th Symposium held in Derby, UK*, ISBN 92-836-0020-7 (Published January 1996).

Adel Ghenaiet received his Ph.D degree from Cranfield University UK in 2001. His area of research and expertise includes erosion of turbomachinery; aerothermodynamic design of turbomachinery; performance and optimization of gas turbine installations and propulsion systems.

Kaddour Touil is a Ph.D student and his research subject concerns CFD of axial turbines.